Under consideration for publication in J. Fluid Mech.

The “zoo” of secondary instabilities precursory to stratified shear flow transition. Part I: shear aligned convection, pairing, and braid instabilities

Supplementary Materials

A. MASHAYEK[1] AND W. R. PELTIER[2]

[1,2]Department of Physics, University of Toronto, Ontario, M5S 1A7, Canada

(Received ?? and in revised form ??)

Throughout this supplementary document, all references to the main document will be prefixed by '$Main-$'.

1. Application of model of Corcos and Sherman (1976)

Figure 1(a) shows the result of the *CS76* calculation for a sample test case characterized by $Ri_0 = 0.08$ for the time at which the cores have grown to their final scales. The streamlines correspond to the final state of the Stuart vortices and the thick black line shows the calculated braid. Panel (b) of the figure shows the evolution of the half thickness of the core (or equivalently the elevation of the tip of the braid). Panel (c) in figure 1 shows the evolution of the stagnation point strain rate for our test case. As we will be primarily interested in studying the secondary instabilities occurring after the primary KH wave has achieved its maximum amplitude, the final value of γ will be used in our calculations. To investigate how the calculations compare to our numerical results, we plot the calculated braid profiles versus the simulated profiles (both at the time of maximum H) in panel (d) of the figure. The solid lines are from *CS76*-type calculations while the dashed lines are for the equivalent braids from the DNS simulations. The arrows in panel (d) indicate the direction of increase in the Richardson number from 0.04 to 0.12, 0.16, and 0.2 respectively. The results presented in the figure demonstrate excellent agreement between the calculations and the simulations. As originally pointed out by *CS76*, the differences between the solid and dashed curves are partly due to simplifications made to obtain equations ($Main-3.5,\ 3.6$) and also to advecting the vorticity field using the simple structure of the Stuart vortices. The increasing difference between the curves for larger values of the Richardson number is derivative of the fact that we have used a value of $\Delta\rho = 2$ in equation ($Main-3.6$). This value is more accurate for small Ri_0 cases than for large. As Ri_0 increases, the time of roll-up of the KH wave to its maximum amplitude increases and hence the density difference across the braid decreases due to the direct influence of diffusion.

2. Heuristic model for vortex core

2.0.1. *Estimating* t_m

Figure 2(a) plots the values of t_m versus the Richardson number for various Reynolds and Prandtl numbers (for the cases listed in $Main-table$ 1). The overlap of essentially all of the curves confirms the Ri_0 -dependence of t_m . The level of stratification of the initial shear layer sets the maximum amplitude that the KH wave can obtain and the time it takes to reach this amplitude. For comparison, t_m calculated based on the *CS76* method is also plotted in the figure (shown by the $-o-$ line). As discussed earlier, evolution timescale is not accurately predicted using their method.

2.0.2. *Estimating* $\Delta\rho_m^{ust}$

The results listed in $Main - table$ 1 for $\Delta\rho_m^{ust}$ are plotted in figure 2(b). The markers on each of the lines in the figure correspond to $Ri(0) = 0.04,\ 0.08,\ 0.12,\ 0.16,$ and 0.2. The figure shows that $\Delta\rho_m^{ust}$ is very close to 2 for small Ri_0 and drops to a value close to 0.5 at $Ri(0) = 0.2$. It also shows that for higher Reynolds and Prandtl numbers, $\Delta\rho_m^{ust}$ decreases less significantly with Ri_0 . So, for very high values of Re and Pr (outside the range covered by the cases explicitly analyzed in our study) it might be safe to assume a value of 2 for $\Delta\rho_m^{ust}$. In our calculations of the Ra^{ust} however, we will use the linear fit

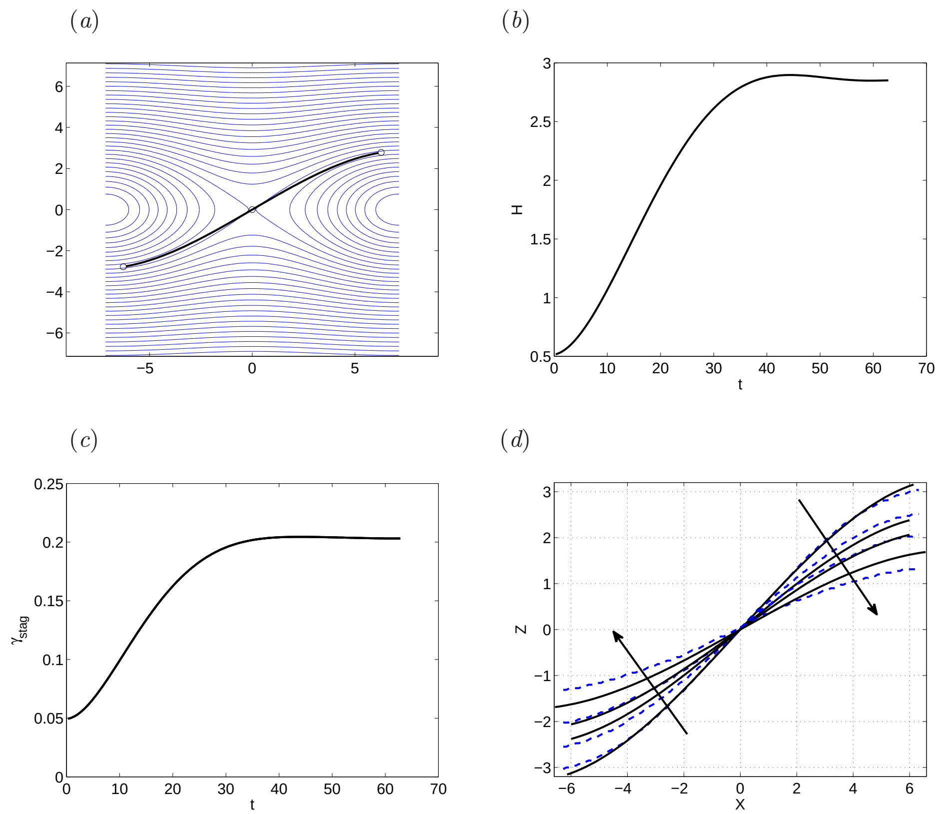

FIGURE 1. (a) Streamlines and braid location obtained from *CS76* calculations for Ri_0 =0.08; (b) Time evolution of the braid elevation H (or half the core thickness) for the case of panel (a); (c) Time evolution of the stagnation point strain rate for the case of panel (a); (d) Comparison of braids calculated using the *CS76* method (solid lines) and braids from simulations at $Re = 1000$ and $Pr = 1$ (dashed lines). The arrows indicate increase in Ri_0 from 0.04 to 0.12, 0.16 and 0.2.

shown in the figure, the equation for which is:

$$\Delta\rho_m^{ust} = 3.22 - 0.024t_m. \tag{2.1}$$

It should be noted that the abscissa in figure 2(b) is labled t_{md} which refers to the time at which $\Delta\rho^{ust}$ peaks. Although table $SM-1$ shows that t_m and t_{md} are close, it is important to note that they are not exactly the same. Figure 3(a) shows the ratio of these two times and indicates that for $0.04 < Ri(0) < 0.16$, it is reasonable to use t_m for t_{md} . This will be our choice as a simplifying step in the analysis to follow. Comparison between the t_m and t_{md} columns in table $Main-table$ 1 shows that the latter is more sensitive to Pr and Re . This is because the time needed by the KH wave to grow to its maximum amplitude is primarily a function of the Richardson number while evolution of the unstable region is affected by the inter-layer diffusion inside the core which itself depends on both Pr and Re .

3. Analysis of the braid

Table 1 shows the results of the theoretical prediction of the braid stagnation point Richardson number versus those obtained from 2D numerical simulations of the table in

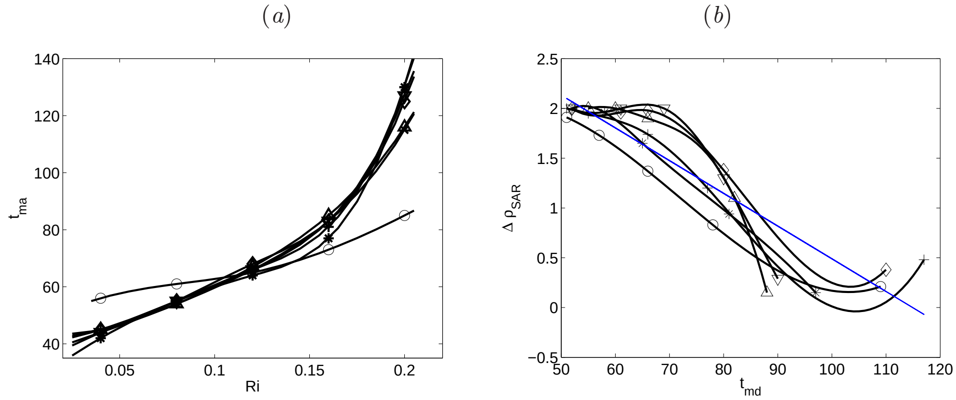

FIGURE 2. (a)Simulation-based results obtained for t_m for $Pr = 1,\ Re = 1000$ (solid line with '+'s), $Pr = 1,\ Re = 2000$ (solid line with '*'s), $Pr = 2,\ Re = 1000$ (solid line with upward triangles), $Pr = 2,\ Re = 2000$ (solid line with downward triangles), $Pr = 4,\ Re = 1000$ (solid line with diamonds) and $Pr = 4,\ Re = 2000$ (solid line with crosses). The solid line with hollow circles shows the t_m results obtained by using the *CS76* model; (b)Simulation-based results for $\Delta\rho_m^{ust}$ versus t_{md} for $Pr = 1,\ Re = 1000$ (solid line with 'o's), $Pr = 1,\ Re = 2000$ (solid line with '+'s), $Pr = 2,\ Re = 1000$ (solid line with '*'s), $Pr = 2,\ Re = 2000$ (solid line with diamonds), $Pr = 4,\ Re = 1000$ (solid line with upward triangles) and $Pr = 4,\ Re = 2000$ (solid line with downward triangles). The solid straight line is a linear fit to all the curves in the figure.

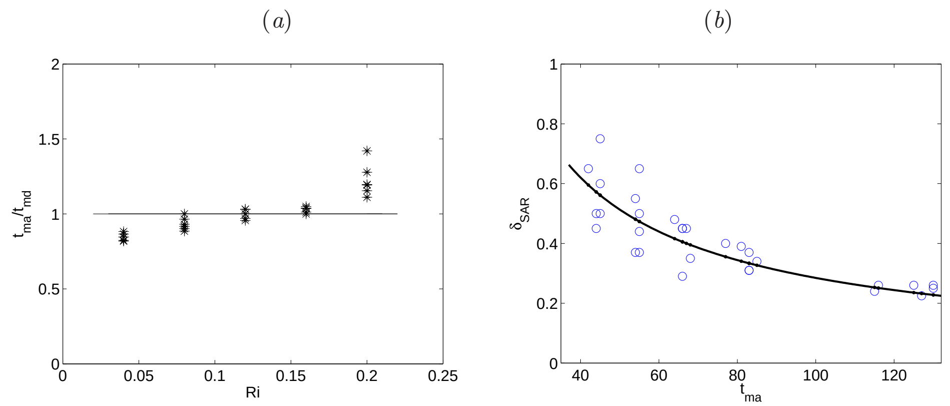

FIGURE 3. (a) t_m/t_{md} plotted for the cases listed in a table in $Main - table$ 1. At each value of Ri_0 , there are six stars corresponding to different Re and Pr ; (b)Data points from the same table (circles) plotted along with correlation $(Main - (3.3))$. The Richardson number increases from 0.04 for the data points at the left to 0.2 for points at the right.

$Main - table$ 1. To obtain theoretical values for Ri_B , we have employed $(Main - 3.9)$ along with γ and ψ obtained using the *CS76* model (using equations $(Main - 3.7,\ 3.8)$. It is important to note that in the analyses of *CS76* leading to relation $SM - (2.1)$, it was assumed that γ could be assumed to be constant along the braid. However, the main equation governing evolution of γ in *CS76* indicates a non-constant value with a peak at the stagnation point. In our analysis, we average γ over the braid and use the result in $(Main - 3.9)$. For comparison between the predictions of $(Main - 3.9)$ and the simulations, we choose the braid Richardson number at the stagnation point (Ri_B^{stag}) in our numerical results and at a time between t_m and the onset of the pairing instability. As we will see, Ri_B^{stag} does not change significantly during this period of time. Table 1 shows that the values of Ri_B^{stag} calculated using the theoretical prediction are in

Case Name	Ri_B theory	Ri_B^{stag} simulation
$c1-1000-0.08$	0.20	0.20
$c1-1000-0.16$	0.12	0.13
$c1-2000-0.08$	0.14	0.15
$c1-2000-0.16$	0.085	0.09
$c1-4000-0.08$	0.10	0.13
$c1-4000-0.16$	0.06	0.04
$c2-1000-0.08$	0.36	0.25
$c2-1000-0.16$	0.21	0.15
$c2-2000-0.08$	0.25	0.19
$c2-2000-0.16$	0.14	0.12

TABLE 1. Ri_B calculated using equation $(Main-3.7)$ in the middle column and from simulations in the right column for sample test cases from $Main-table\ 1$

good agreement with our 2D numerical simulations. The agreement however diminishes with an increase in the Prandtl number. This is probably because, for higher Prandtl numbers, the strength of the vorticity bands in the cores is increased compared to that for the lower Prandtl number cases. Hence, the effect of the flow field of the cores on the braid at the stagnation point is more pronounced for cases with $Pr = 2$. As the theoretical prediction totally ignores this effect, the agreement between the theory and the simulations deteriorates at higher Prandtl numbers. Nevertheless, the results are still in reasonable agreement for $Pr = 2$.

3.1. *Diagnostic tools for the braid*

To facilitate our analyses of the braid, we needed to develop certain diagnostic tools. To explain development of the tools, we consider the case c1-2000-0.12 as an example. Figure 4 shows the vorticity field at a sequence of times in the evolution of this flow.

To extract braid information from the simulations, we extracted data from one hundred traverses between the centers of the cores for each time frame of each simulation. The point of maximum vorticity on each traverse was then identified to define the location of the braid center. Alternatively, one could use the density profiles to locate the center of the braid. Connecting the 100 points obtained in this fashion provided a braid profile for each time frame. The solid lines in Figure 5(a) present the results for three different times for the same test case as illustrated in Figure 4. The solid lines in the figure are overlain by a third-order polynominal fit shown as the dash-dotted curve. For times shown in panel (a), the braid profiles and the fits coincide closely. Panel (b) illustrates the braid at a sequence of later times when the braid deformation is pronounced and so the fits do not coincide with the earlier braid profiles. For these cases, the fits (dash-dotted lines) can be treated as an unperturbed braid, or in other words, as the braid had it had no secondary braid instabilities deforming it. Therefore, for the cases of panel (b), the deviation of the braids from the polynominal fits can be considered a measure of the braid deformation. We have calculated the area between the solid and dash-dotted curves for each time step and we employ the difference to define the "braid deformation". For the test case under consideration, this braid deformation is plotted in panel (c) of Figure 4. At early times when the braid has yet to become deformed, this parameter has a value near zero. However, at a time shortly before $t = 80$, the braid begins to grow (as shown in Figure 4 $(d-e)$). At a time slightly prior to $t = 90$, small billows form on the braid and these

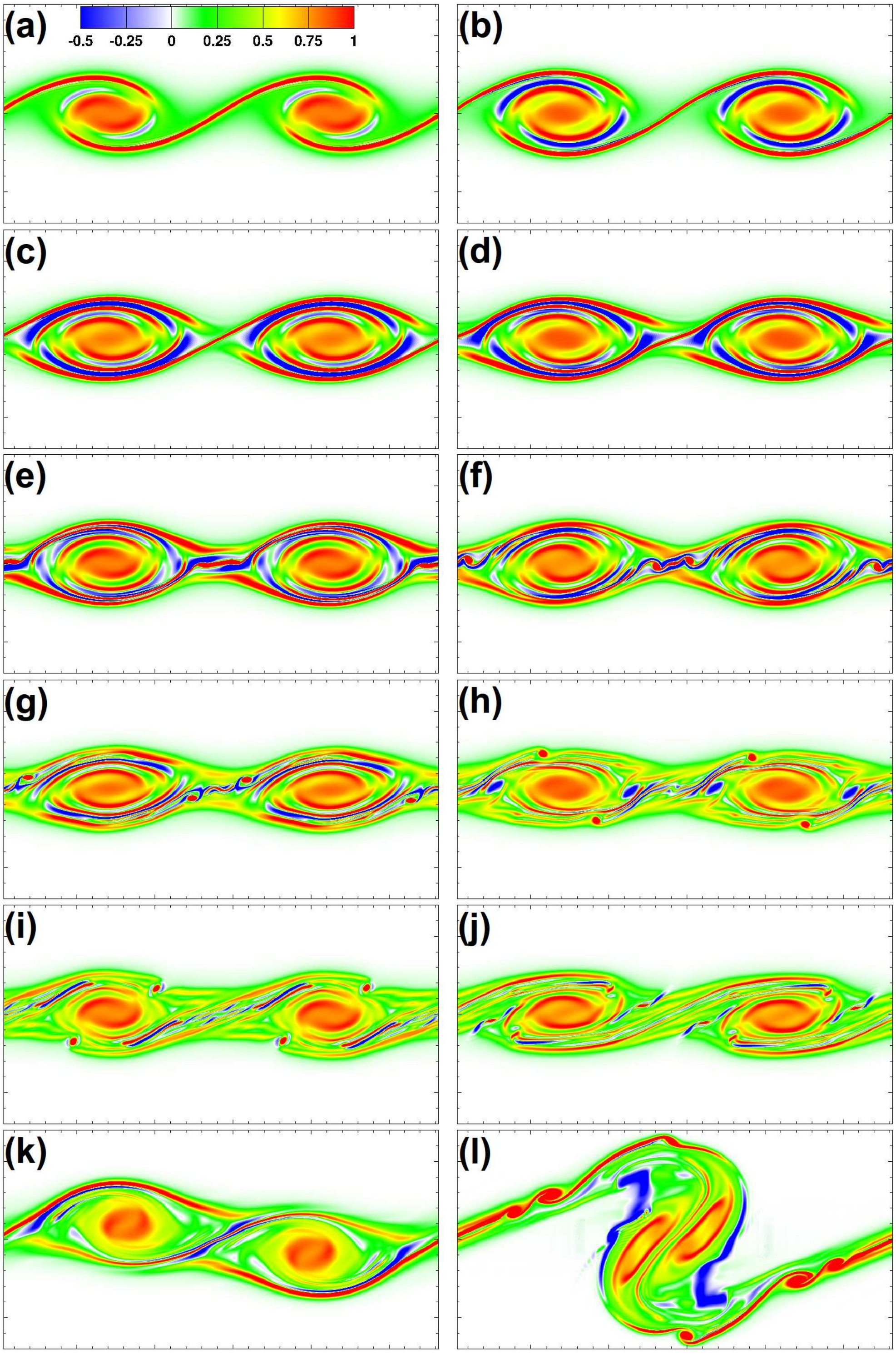

FIGURE 4. Vorticity contours for case c1-2000-0.12 and at times (*a*) t=50, (*b*) t=60, (*c*) t=75, (*d*) t=80, (*e*) t=85, (*f*) t=90, (*g*) t=95, (*h*) t=100, (*i*) t=105, (*j*) t=110, (*k*) t=140, (*l*) t=165.

appear in the form of small peaks on the braid deformation plot. The larger deformations at later times in panel (c) of figure 5 are associated with the pairing process. Comparing panels (a, b) shows that despite the braid deformation, its location does not vary much for times beyond $t = 50$.

Panel (d) of Figure 4 shows the braid thickness calculated from the vorticity field (solid line) and the density field (dashed line). We define the braid vorticity thickness as twice the normal-to-braid distance of the center of the braid from the location where the vorticity has a value of about 10% of the difference between the maximum value (at the center of the braid) and the minimum value of approximately zero (sufficiently far from the braid). The density thickness is defined in a similar fashion. This definition of the thickness based upon the 10% criteria is somewhat arbitrary and a more accurate definition is that proposed in *S03*. However, we are primarily interested in braid location and changes in thickness not the value of braid thickness itself. As shown in the figure, there is a period of time between $t = 50$ and $t = 85$ when the braid is in a stable condition and its thickness is unchanging. As we will see, the value of Ri_B is also relatively stable during this period and, if it is sufficiently low, we may anticipate the emergence of secondary shear instability of the braid. The ratio of the braid's vorticity thickness to its density thickness is also close to unity during the semi-equilibrium phase which is in agreement with the results of *S03* for $Pr = 1$.

Panel (e) plots the parameter δ_{pair} which is the horizontal distance between the tips of the strong vorticity layers in two neighbour cores (shown in panels ($b - d$) of Figure 4). As mentioned previously, the time at which these bands meet and thereafter drain the vorticity from the braid is of critical importance as it marks the onset of the growth of various secondary instabilities. As panel (e) of Figure 5 shows, at a time shortly after $t = 80$, δ_{pair} drops to zero and it is at this time that we observe the braid deformation to begin to grow in panel (c). This time also marks the onset of the merging instability. To demonstrate this, we plot Δz_{core} in panel (f) which is the difference between the vertical positions of tops of the left and right cores. Prior to the onset of merging, the two positions are identical and Δz_{core} is zero but this grows slowly after δ_{pair} vanishes implying that pairing is underway. Although the coincidence of the time of $\delta_{pair} = 0$ and the onset of $\Delta z_{core} > 0$ occurs in many of our simulations, in general, the pairing instability may get underway even before δ_{pair} vanishes depending on the flow initialization. Moreover, $\delta_{pair} = 0$ is not a necessary condition for the merging instability. At high Richardson numbers (0.2 and higher) merging may be completely prohibited by the influence of the density stratification.

Panel (g) of Figure 4 presents time variation of the vertical extent of the core, D_{core}, demonstrating that it oscillates about the mean for a time but is thereafter affected by the onset of secondary instabilities that originate on the braid and by the pairing process. Panel (h) plots the variation of Ri_B at the stagnation point. During the period when the braid is approximately steady ($t \sim 50 - 85$), the Ri_B^{stag} is essentially constant. Near $t = 85$ when δ_{pair} vanishes and the braid is drained of its vorticity, its Richardson number drops very rapidly and secondary vortices appear on the braid. The large variations for $t > 100$ in panel (h) are due to the merging process. A more detailed examination of Ri_B may be constructed by plotting it as a function of position along the braid. This is done in panels (i) and (j) for various times. For earlier times and before δ_{pair} tends to zero, the minimum value of Ri_B obtains at the stagnation point. However, as $\delta_{pair} \to 0$, at the locations where the tips of the cores outermost negative vorticity bands meet the braid, Ri_B is further reduced. This is clearly seen for times $t \geqslant 75$. The two points of contact have a near zero Richardson number at $t = 85$ which is near the time that secondary vortexes form at those points on the braid. The horizontal axes in panels (i)

and (j) denote the global x-direction and not the along-braid coordinate. The diagnostic tools described above (specially those employed to construct panels (c) through (f)) are useful for determining conditions under which the emergence of small and large scale deformations on the braid and cores appear. We will further employ these tools in our analyses in the next sections and we will also construct similar plots to those shown in figure 5 for the cases to be considered.

4. Details of the Non-Separable Stability Analysis

To convert the system of equations into an eigensystem, we expand the perturbations via the Galerkin method (see *KP85* for details) using the expansions

$$\hat{u} = \sum_{\lambda=-L}^{L}\sum_{\nu=0}^{N} u_{\lambda\nu}F_{\lambda\nu}, \quad \hat{w} = \sum_{\lambda=-L}^{L}\sum_{\nu=0}^{N} w_{\lambda\nu}G_{\lambda\nu}, \tag{4.1}$$
$$\hat{\rho} = \sum_{\lambda=-L}^{L}\sum_{\nu=0}^{N} \rho_{\lambda\nu}G_{\lambda\nu}, \quad \hat{p} = \sum_{\lambda=-L}^{L}\sum_{\nu=0}^{N} p_{\lambda\nu}G_{\lambda\nu},$$

where

$$F_{\lambda\nu} = e^{i\lambda\alpha x}\cos\frac{\nu\pi z}{H}, \quad G_{\lambda\nu} = e^{i\lambda\alpha x}\sin\frac{\nu\pi z}{H}. \tag{4.2}$$

We next substitute (4.1) into the system of equations $main-(4.4)$, $main-(4.6)$, $main-(4.7)$ and $main-(4.9)$ and diagonalize the left hand side of the system by taking proper inner products. Then we solve equation $main-(4.9)$ for $p_{\lambda\nu}$ and the result is substituted into $main-(4.4)$ and $main-(4.6)$. This leads to a set of linear algebraic equations for the coefficients $\hat{u}$, $\hat{w}$ and $\hat{\rho}$ as

$$\sigma u_{\kappa\mu} =< UU >_{\kappa\mu}^{\lambda\nu} u_{\lambda\nu}+ < UW >_{\kappa\mu}^{\lambda\nu} w_{\lambda\nu}+ < UT >_{\kappa\mu}^{\lambda\nu} \rho_{\lambda\nu}, \tag{4.3}$$
$$\sigma w_{\kappa\mu} =< WU >_{\kappa\mu}^{\lambda\nu} u_{\lambda\nu}+ < WW >_{\kappa\mu}^{\lambda\nu} w_{\lambda\nu}+ < WT >_{\kappa\mu}^{\lambda\nu} \rho_{\lambda\nu}, \tag{4.4}$$
$$\sigma \rho_{\kappa\mu} =< TU >_{\kappa\mu}^{\lambda\nu} u_{\lambda\nu}+ < TW >_{\kappa\mu}^{\lambda\nu} w_{\lambda\nu}+ < TT >_{\kappa\mu}^{\lambda\nu} \rho_{\lambda\nu}. \tag{4.5}$$

The expressions for the $< >_{\kappa\mu}^{\lambda\nu}$ terms are long and can be found in the appendix of Smyth & Peltier (1991). The system of equations (4.3), (4.4) and (4.5) can be compiled into the form $\sigma V_i = A_{ij}V_j$, where A is a constant matrix and V is the concatenation of $u_{\lambda\nu}$, $w_{\lambda\nu}$ and $\rho_{\lambda\nu}$. Eigenvalues of A are computed using exactly the same methods employed in by Klaassen & Peltier (1985).

The truncation level N for the Galerkin expansions in (4.1) is chosen based on the scheme proposed by *KP85*, namely:

$$L(\nu) = \left[\frac{N-\nu}{2} - \frac{b}{\alpha}\right]. \tag{4.6}$$

where the square brackets mean "the largest integer not exceeding the value of the enclosed quantity" and N should be an odd integer. The value of N is limited by two factors: 1- The limited memory of the machines used to solve the eigensystem and 2- human labour. Although the memory of machines available to us allows for a very large N for the stability analysis at one instant for one case, we are interested in performing the analysis for various times during the evolution of each case and we need to cover the several cases in this paper and the companion paper Mashayek & Peltier (2012). Hence, the value of N affects the overall time of our calculations greatly.

More importantly, one has to note that the Reynolds and Prandtl numbers that we

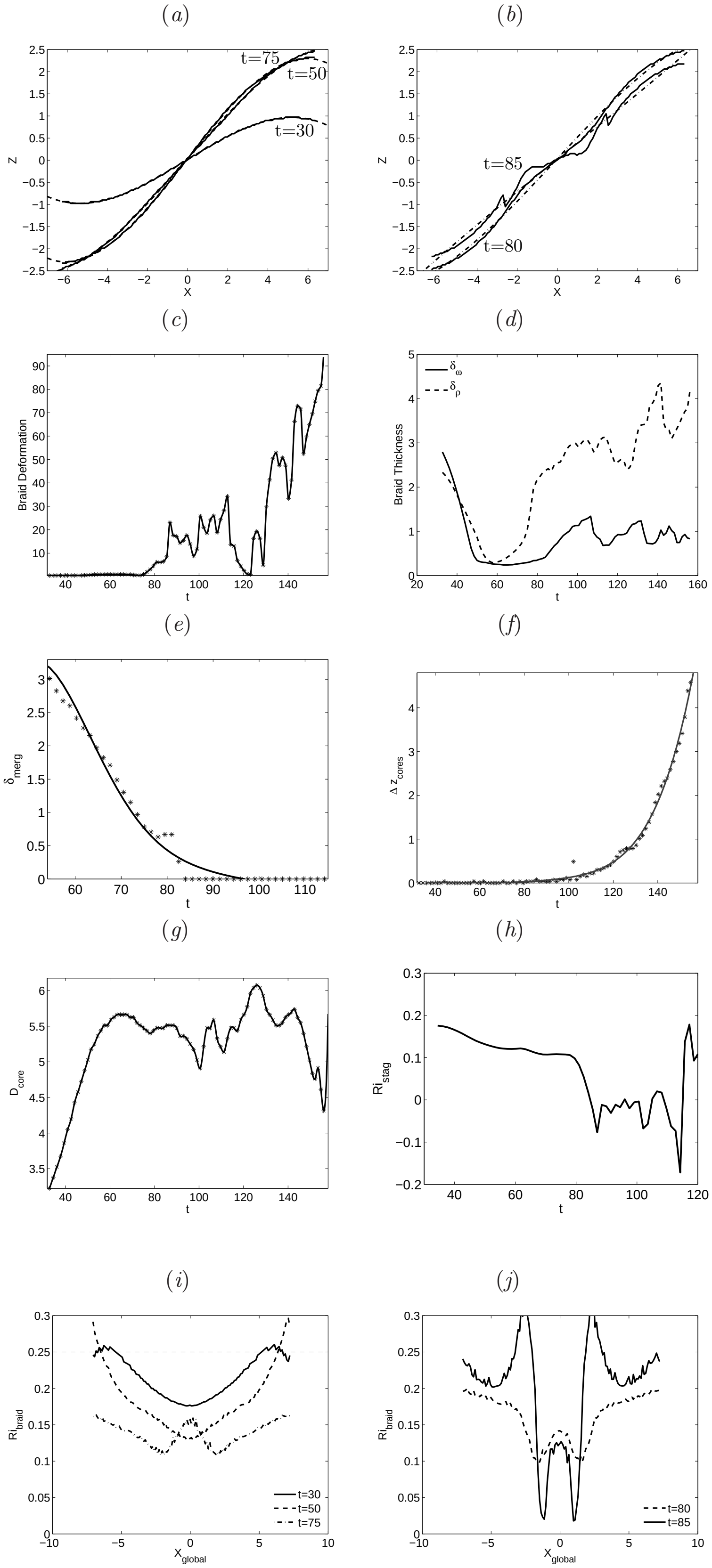

FIGURE 5. Flow diagnostic tools for case c1-2000-0.12. (*a*) Braid location at times $t = 30,\ 50,\ 75$; (*b*) braid location at times $t = 80,\ 85$; (*c*) braid deformation; (*d*) braid thickness calculated from the vorticity and the density fields; (*e*) δ_{pair}; (*f*) Δz_{cores}; (*g*) D_{core}; (*h*) Ri_B at the stagnation point; (*i*) Ri_B along the braid for $t = 30, 50,\ 75$; (*j*) Ri_B along the braid for $t = 80, 85$.

are interested in are considerably higher than those considered in the earlier studies of *KP85*, Klaassen & Peltier (1991), Klaassen & Peltier (1989) and Smyth & Peltier (1991). As a result, we detect more secondary instabilities some of which exist over a wide range of spanwise wavenumbers, are of oscillatory nature, and persist over long periods of flow evolution. This translates to detection of a large number of 'new' eigenvalues in our analysis. Since identification of the type of each eigenvalue is achieved through the calculation of its corresponding eigenfunction, and since that calculation depends directly on both N and the resolution of our simulations (which are relatively high), the stability analysis we perform involves a tedious mode-finding and mode-tracking procedure. Therefore, N has to be chosen to be sufficiently large but not excessively so. We determine this limit by increasing N from a small value to large until we no longer observe any significant difference in the instability modes detected and in their growth rates. For all the cases considered in this paper and in the companion paper MP2, we found $N = 37$ (for one wavelength of the primary KH wave) to satisfy this criterion.

REFERENCES

Klaassen, G.P. & Peltier, W.R. 1985 The onset of turbulence in finite amplitude kelvin-helmholtz billows. *J. Fluid Mech.* **155**, 1–35.

Klaassen, G.P. & Peltier, W.R. 1989 The role of transverse secondary instabilities in the evolution of free shear layers. *J. Fluid Mech.* **202**, 367–402.

Klaassen, G.P. & Peltier, W.R. 1991 The influence of stratification on secondary instabilities in free shear layers. *J. Fluid Mech.* **227**, 71–106.

Mashayek, A. & Peltier, W.R. 2012 Secondary instabilities of parallel stratified shear layers. part ii: Effect of stratification. *J. Fluid Mech.* **submitted**.

Smyth, W.D. & Peltier, W.R. 1991 Instability and transition in finite amplitude kelvin-helmholtz and holmboe waves. *J. Fluid Mech.* **228**, 387–415.